Article ID: 1000-7032(2025)01-0140-16

Development of NIR Responsive Upconversion Nanosensor for Turn-on Detection of 4-Nonylphenol

HUANG Sili[1], XU Kuncheng[1], YE Yiwen[1], WEN Hongli[1,2*], CHEN Rihui[1], SONG Wei[3], CHEN Wei[4*], ABDUR Raheem Aleem[1,5*]

(1. *Key Laboratory of Clean Chemistry Technology of Guangdong Regular Higher Education Institutions, Guangdong Engineering Technology Research Center of Modern Fine Chemical Engineering, School of Chemical Engineering and Light Industry, Guangdong University of Technology, Guangzhou* 510006, *China*;
2. *Guangdong Provincial Laboratory of Chemistry and Fine Chemical Engineering Jieyang Center, Jieyang* 515200, *China*;
3. *Analysis and Test Center, Guangdong University of Technology, Guangzhou* 510006, *China*;
4. *School of CHIPS, Xi'an Jiaotong-Loverpool University, Suzhou* 215123, *China*;
5. *Zhejiang Provincial Engineering Research Center of New Technologies and Applications for Targeted Therapy of Major Diseases, College of Life Sciences and Medicine, Zhejiang Sci-Tech University, Hangzhou* 310018, *China*)

* *Corresponding Authors, E-mail: hongliwen@gdut. edu. cn; Wei. Chen*03*@xjtlu. edu. cn; abdurraheemalem@hotmail. com*

Abstract: 4-Nonylphenol (NP) is a kind of estrogen belonging to the endocrine disrupter, widely used in various agricultural and industrial goods. However, extensive use of NP with direct release to environment poses high risks to both human health and ecosystems. Herein, for the first time, we developed near-infrared (NIR) responsive upconversion luminescence nanosensor for NP detection. The Förster resonance energy transfer based upconversion nanoparticles (UCNPs)-graphene oxide sensor offers highly selective and sensitive detection of NP in linear ranges of 5-200 ng/mL and 200-1 000 ng/mL under 980 nm and 808 nm excitation, respectively, with LOD at 4. 2 ng/mL. The sensors were successfully tested for NP detection in real liquid milk samples with excellent recovery results. The rare-earth fluoride based upconversion luminescence nanosensor with NIR excitation wavelength, holds promise for sensing food, environmental, and biological samples due to their high sensitivity, specific recognition, low LOD, negligible autofluorescence, along with the deep penetration of NIR excitation sources.

Key words: Er^{3+}/Yb^{3+}/Nd^{3+}; upconversion nanoparticles; Förster resonance energy transfer; estrogen; detection
CLC number: O482. 31 **Document code**: A
DOI: 10. 37188/CJL. 20240187 **CSTR**: 32170. 14. CJL. 20240187

近红外响应上转换荧光纳米传感器用于4-壬基苯酚检测

黄丝丽[1], 许坤城[1], 叶依文[1], 温红丽[1,2*], 陈日晖[1], 宋 巍[3], 陈 伟[4*], ABDUR Raheem Aleem[1,5*]

(1. 广东工业大学 轻工化工学院, 广东省教育厅清洁化学技术重点实验室, 广东省现代精细化工工程技术研究开发中心, 广东 广州 510006;
2. 化学与精细化工广东省实验室揭阳分中心, 广东 揭阳 515200;
3. 广东工业大学 分析测试中心, 广东 广州 510006;
4. 西安交通-利物浦大学 芯片学院, 江苏 苏州 215123;

收稿日期: 2024-08-11; **修订日期**: 2024-09-02
基金项目: 国家自然科学基金(22075052); 广东省基础与应用基础研究基金(2023A1515012988); 广东省省级科技计划项目(2022A0505020005); 江苏省教育厅项目(EFP10120240023)
Supported by National Natural Science Foundation of China(22075052); Guangdong Basic and Applied Basic Research Foundation (2023A1515012988); Science and Technology Planning Project of Guangdong Province(2022A0505020005); Project from the Department of Education at Jiangsu Province for the School of CHIPS at XJTLU(EFP10120240023)

5. 浙江理工大学 生命科学与医药学院, 重大疾病靶向治疗新技术和应用浙江省工程研究中心, 浙江 杭州　310018)

摘要: 4-壬基苯酚(NP)是一种雌激素,属于内分泌干扰物,广泛应用于各种农业和工业品。然而,NP的过度使用及直接释放到环境中,会对人类健康和生态系统造成高风险。在此,我们首次研究了近红外(NIR)响应的上转换荧光纳米传感器用于4-NP的检测。基于Förster共振能量传递的上转换纳米颗粒(UCNPs)-氧化石墨烯传感器具有高选择性和高灵敏度,在980 nm和808 nm激发下,对NP的线性检测范围分别为5~200 ng/mL和200~1 000 ng/mL,LOD为4.2 ng/mL。该纳米传感器在实际液体牛奶样品中成功进行了NP检测,结果令人满意。近红外激发的稀土氟化物基上转换荧光纳米传感器由于具有高灵敏度、高特异性识别、低LOD、无自发荧光以及近红外激发源的穿透能力强,在食品安全检测、环境监控和生物样品中具有很好的应用前景。

关　键　词: $Er^{3+}/Yb^{3+}/Nd^{3+}$; 上转换纳米颗粒; Förster共振能量传递; 雌激素; 检测

1　Introduction

4-Nonylphenol (NP) is a kind of estrogen and belongs to the endocrine disrupters that is extensively used in industry, agriculture, and human life as an antistatic agent, plasticizer and emulsifier[1]. Extensive usage of NP with direct release to environmental systems poses high risks to both ecosystems and human health[2]. As a result, there is a considerable possibility that NP will enter the food chain and being consumed by animals as well as humans[3]. Humans probably suffer due to the acute NP inhalation or intake which leads to a variety of physiological symptoms, including anxiety and depression[4-5]. Long-term consumption of NP could cause breast cancer, severe damage to the kidneys, liver, reproductive and neurological systems[2, 6-7]. NP is classified as a hazardous waste by the US Environmental Protection Agency (EPA)[3,8]. Therefore, it is urgent and crucial to design a fast, accurate and ultrasensitive technique for NP residue detection in food and aqueous environment.

Several typical techniques, such as liquid chromatography-mass spectrometry[9], gas chromatography-mass spectrometry[10], high-performance liquid chromatography[11], high-performance liquid chromatography-ultraviolet (UV) detector[12], high-performance liquid chromatography-fluorescence detector[13], and electrochemical biosensors[14] have been developed for the quantitative detection of NP. However, due to quick response time, ease of use, real-time sensing, portability and high sensitivity for NP estrogen detection, fluorescent sensors have attracted more attention than the above-mentioned analytical approaches[6,15]. For example, Tu *et al.* [16] presented phosphorus and nitrogen co-doped carbon dots which exhibited blue fluorescence emission at 444 nm under 356 nm excitation and obtained a limit of detection (LOD) of 78.62 nmol/L for NP. Jiang *et al.* [17] developed a fluorescent sensor based on quantum dots (QDs) capped with molecular imprinted polymer (MIP) using 3-aminopropyltriethoxysilane and tetramethoxysilane as the functional monomer and the cross-linker, respectively. The MIP-coated QDs fluorescent sensor exhibited quenched emission at 545 nm under 320 nm excitation with presence of NP, achieving linear NP concentration range of 1−30 μmol/L with LOD of 0.04 μmol/L. The commonly used inorganic QDs exhibit chemically unstable and photo-blinking effects[18]. Moreover, the primary shortcoming of the fluorophores is that the excitation wavelength typically in the UV-visible range[19], and the sensitivity of the detection will be affected by the biomolecule-derived background fluorescence[20].

The rare earth-doped upconversion nanoparticles (UCNPs) have the ability to absorb low-energy near-infrared (NIR) photons (*e. g.*, 980 nm) and emit luminescence of the higher energy photons in UV-visible range[21-22]. UCNPs offer various benefits as optical sensors because of excellent photo and chemical stability, large anti-Stokes shift, low toxicity, strong upconversion luminescence (UCL), narrow emission bandwidth, long lifetime and ease of surface modification[18, 23]. In comparison with UV-visible excitation, biomolecular autofluorescence is

avoided at NIR excitation wavelengths, and light scattering is reduced[24-25]. Due to the above-mentioned advantages, UCNPs have been widely explored in a variety of applications including anti-counterfeiting, bioimaging, drug delivery, 3D printing and biosensing[26-31]. Generally, UCNPs based on Yb^{3+} sensitization is capable to upconvert 980 nm irradiation to UV-visible range emission. On the other hand, Nd^{3+}-sensitized UCNPs exhibit not only efficient UCL upon 808 nm laser excitation but also advantages of non-overheating effect and significantly improved penetration depth for biological samples[32]. Therefore, Nd^{3+} and Yb^{3+}-sensitized UCNPs offered the NIR excited efficient UCL and can be potentially applied in fluorescent bioimaging, photodynamic therapy and biomedical sensing[33-34].

The UCNPs with the preparation mostly in organic solvents are capped with oleate (OA) ligands which make these nanomaterials hydrophobic[35]. Accordingly, surface modification of the nanomaterials from hydrophobic to hydrophilic is required before continuing aqueous environment sensing and biological application of UCNPs[36]. The silica (SiO_2) inert shell offers numerous advantages for optical bioanalytical applications, including hydrophilicity, non-toxicity, excellent biocompatibility and the availability of various functional groups binding sites which are crucial for further functionalization[37]. Amino ($—NH_2$) functionalized SiO_2 layer coated on the UCNPs surface allows for water dispersion as well as offers reactive functional moieties for subsequent conjugation with biomolecules (*i. e.*, DNA or RNA)[38]. The functional SiO_2-modified UCNPs have been applied in numerous practical applications such as photodynamic therapy, cellular imaging, biosensing and drug delivery[39-41]. Recently, Tong *et al.* [42] proposed the application of $NaYF_4$: Er, Yb UCNPs@SiO_2 in water-soluble ink printing for anti-counterfeiting. Sun *et al.* [41] designed a nanosensor based on energy transfer from $NaYF_4$: Yb, Er@$NaYF_4$ UCNPs coated with NH_2-functionalized SiO_2 layer to gold nanoparticles for the sensing of cadmium and glutathione ions.

As single-stranded oligonucleotide (DNA or RNA) that mimics monoclonal antibodies, aptamers are powerful for specific binding to its preselected targets[43]. Aptamers are screened by Systematic Evolution of Ligands by Exponential Enrichment (SELEX) method[44]. The advantages of aptamers over antibodies include excellent binding affinity, pronounced specific recognition, long-term stability for preservation, convenience for carriage, ease of modification, low cost, minimal differences between batches, and wide target range[45]. Graphene oxide (GO) has promising characteristics as an excellent quencher when considering a potential candidate for energy acceptors because of its high surface area, high solubility in water and unique affinity to diverse biomolecules[46-47]. For instance, single-stranded oligonucleotides (such as aptamer) are attached on the surface of GO *via* π-π stacking interactions[48]. As a fluorescent acceptor, GO has a large specific surface area and a highly efficient quenching ability which makes it a suitable and highly efficient quencher of UCNPs[49]. For example, Gonzalez *et al.* [50] demonstrated efficient energy transfer between UCNPs and GO sheets due to excitation and emission absorption by GO sheets and Förster resonance energy transfer (FRET), with the former as the major UCL quenching mechanism. Li *et al.* [51] presented the Tween 20 modified GO and specific aptamer-based fluoresce sensor for the detection of ochratoxin A, revealing 5–200 nmol/L linear detection range with LOD of 3.12 nmol/L.

Herein, for the first time, we develop rare-earth fluoride UCNPs based biosensor with NIR excitation for the ultra-sensitive sensing of NP estrogen through FRET (Fig. 1). The prepared OA capped $NaYF_4$: Yb/Er@$NaYF_4$: Nd core-shell UCNPs (UCNPs-OA) were functionalized with amino-SiO_2 layer to obtain the hydrophilic nanoparticles (UCNPs@SiO_2-NH_2) and subsequent aptamer conjugation (UCNPs@SiO_2@apt). The UCNPs acted as an efficient energy donor and GO nanosheets as an ideal energy quencher. The UCNPs@SiO_2@apt attached onto the surface of GO nanosheets *via* π-π stacking interactions, resulting in the UCL quenching through FRET from UCNPs to GO nanosheets[52]. When NP

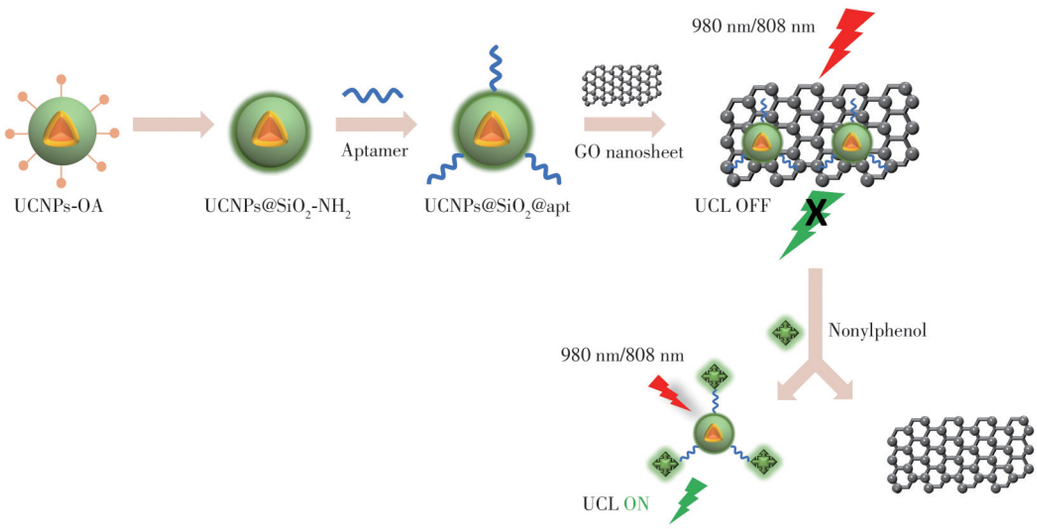

Fig.1　Schematic diagram of NIR excitable UCNPs@SiO_2@apt-GO biosensor based on FRET for highly sensitive and selective sensing of NP

estrogen was introduced to the UCNPs@ SiO_2@ apt-GO sensor, aptamer preferentially combined with NP, causing the detachment of UCNPs@ SiO_2@apt from GO nanosheets, and simultaneous enabling the recovery of UCL. Moreover, 980 nm excited UCNPs@SiO_2@apt-GO sensor was applied for the determination of NP estrogen in liquid milk samples with acceptable results. Thus, the rare-earth fluoride based and NIR excitable UCNPs@ SiO_2@apt-GO sensor is promising for turning-on biosensing of NP estrogen with high sensitivity and excellent selectivity.

2　Experiment

2.1　Regents and Materials

The chemicals with satisfactory purities were utilized as obtained without having additional purification. $Yb(CH_3CO_2)_3 \cdot xH_2O$ (99.9%), $Y(CH_3CO_2)_3 \cdot xH_2O$ (99.9%), $Er(CH_3CO_2)_3 \cdot xH_2O$ (99.9%), $Nd(CH_3CO_2)_3 \cdot xH_2O$ (99.9%), NH_4F (98%), glutaraldehyde (25% in aqueous solution), oleic acid (90%), 1-octadecene (90%) and NaOH (>98%) were supplied from Sigma-Aldrich. Tetramethylammonium hydroxide (25% in aqueous media), (3-aminopropyl) triethoxysilane (APTES, 98%), tetraethyl orthosilicate (TEOS) (99%), methanol (99.5%), cyclohexane (99.5%), NP (98%), bisphenol A (BPA, 99%), phenylphenol (PP, 98%), di-2-ethylhexyl phthalate (DEHP, 99%), phenol (PHE, 99%) standards were supplied from Aladdin, China. Graphene oxide (GO, size 0.5-5 μm) was purchased from the Xianfeng Nano Co. Ltd., China. Ammonium hydroxide solution (GR, 25%-28%) was purchased from the Macklin, China. Milk (liquid) was obtained by Walmart Guangzhou, China. The NP-specific aptamer sequence was 5'-NH_2-ATG CGG ATC CCG CGC GGC CGG CCA GTG CGC GAA GCT TGC GC-3' and supplied by Bio-Tech Co. Ltd., Shanghai China[53]. The milli-Q ultrapure water was utilized in all the experiments. The membrane with 0.22 μm pore size was supplied by the Jinteng Co., Ltd., Tianjin, China.

2.2　Characterizations

The size and morphological changes of the nanoparticles were determined using a Hitachi HT7700 transmission electron microscope (TEM) operating at 100 kV. Elemental mapping was conducted using the FEI TALOS F200S high-resolution transmission electron microscope (HRTEM) in scanning transmission electron microscopy operating at 200 kV. Using Cu Kα irradiation (λ = 0.154 06 nm), crystalline phases were identified using a Malvern Panalytical DY735 X-ray diffractometer with a scanning rate of 5(°)·min^{-1} and 2θ range of 10°-80°. Fourier transform infrared (FT-IR) spectra were obtained at a resolution of 1 cm^{-1} and from 400 cm^{-1} to 4 000 cm^{-1} using a Thermo-Fisher Scientific

spectrometer of Nicolet 6 700 following the KBr pellet approach. Shimadzu UV2700 spectrophotometer was utilized to recorded ultraviolet-visible (UV-Vis) spectra. Zeta potentials were measured by Malvern Zeta potential analyzer. Measurements of contact angles were carried out using OCA100 (Dataphysics, Germany) apparatus with a 3 μL droplet placed over a specific quantity of powdered samples. A Ocean Optics spectrometer of USB 2000+ and HORIBA Jobin Yvon fluorescence spectrometer of FluoroMax-4 were used to record UCL spectra by using an external fiber coupled diode 980 nm and 808 nm laser (BWT Beijing Ltd.), respectively.

2.3 Synthesis of Core and Core-shell Nanoparticles

The $NaYF_4$: Yb/Er (20%/2% (mole fraction)) core nano-particles were synthesized through facile method described in previous report[35]. Briefly, 2 mL of $Yb(CH_3COO)_3$ (0.2 mol/L), $Y(CH_3COO)_3$ (0.2 mol/L) and $Er(CH_3COO)_3$ (0.2 mol/L) were blended in 50 mL flask with 6 mL of 1-octadecene and 4 mL of oleic acid under continuous stirring. After 30 min of constant stirring and heating at 160 ℃, solution was cooled to room temperature. The combined solution was stirred at 50 ℃ for 30 min with addition of NH_4F (1.54 mmol) and NaOH (1 mmol) solution in methanol. The solution was initially heated at 110 ℃ for methanol evaporation and then under argon atmosphere heated at 300 ℃ for 1 h. The final sample was washed with ethanol, methanol and cyclohexane several times and kept at 4 ℃ after dispersed in 4 mL cyclohexane.

Similarly, $NaYF_4$: Yb/Er (20%/2%) @$NaYF_4$: Nd (40%) core-shell UCNPs was synthesized using the above-mentioned method except for the 2 mL of $Y(CH_3COO)_3$, $Yb(CH_3COO)_3$ and $Er(CH_3COO)_3$ were exchanged with $Y(CH_3COO)_3$ and $Nd(CH_3CO_2)_3$. As-prepared core nanoparticles (3.9 mL) was added along with NH_4F (1.54 mmol) and NaOH (1 mmol) methanol mixture. The resultant OA capped core-shell $NaYF_4$: Yb/Er@$NaYF_4$: Nd UCNPs (denotes as UCNPs-OA) were dispersed in cyclohexane (3.9 mL).

2.4 Amino-SiO_2 Modification of Core-shell UCNPs

UCNPs-OA surface was coated with amino-SiO_2 using an approach previously reported[52,54]. Firstly, UCNPs-OA (3 mL in cyclohexane) were centrifuged and dispersed again in 60 mL of ethanol following 40 min sonication in a 250 mL flask at room temperature. The mixture was stirred and heated to 42 ℃ with the addition of $NH_3 \cdot H_2O$ (2.5 mL) and ultrapure water (20 mL). Then, 60 μL of TEOS was added to the above mixture, and the mixture was stirred for 6 h at 42 ℃ to coat core-shell UCNPs with SiO_2 layer (UCNPs@SiO_2). The mixture was heated at 42 ℃ for 6 h after 100 μL of APTES was added, and then it was allowed to cool to room temperature. The final sample was centrifuged at 8 500 r/min (7 672.8 × g) for 30 min and after several times washing, redispersed it in ethanol and stored in a fridge at 4 ℃ to obtain the amino-SiO_2 modified core-shell UCNPs (UCNPs@SiO_2-NH_2).

2.5 Preparation of Aptamer Conjugated Core-shell UCNPs

The aptamer conjugated UCNPs@SiO_2-NH_2 were obtained by using standard glutaraldehyde approach with modifications[52]. To chemically activate amino group on the surface, UCNPs@SiO_2-NH_2 (4 mg) were sonicated in ultrapure water for 10 min, and then added with 0.25 mL of glutaraldehyde aqueous solution with the mixture kept for 2 h continuous shaking at room temperature. The above-mentioned sample was centrifuged at 8 500 r/min (5 023.6 × g) for 10 min and after several times washing, dispersed aging in water. For UCNPs@SiO_2-NH_2 conjugation with aptamer (UCNPs@SiO_2@apt), 5.4 nmol of aptamer was added to the obtained solution of UCNPs@SiO_2-NH_2 with amino group activated by glutaraldehyde under overnight shaking at room temperature. The resultant blend was centrifuged for 10 min at 8 500 r/min (5 023.6 × g) to attain UCNPs@SiO_2@apt that was washed twice and dispersed again in ultrapure water. UCNPs@SiO_2@apt were kept in storage at 4 ℃.

2.6 Experimental Procedures for NP Sensing

The NP detection experimental conditions were

set appropriately. Firstly, UCNPs@SiO_2@apt (0.2 mg/mL) and GO nanosheets (0.3 mg/mL) were incubated at different time with an excitation wavelength of 980 nm. Secondly, the optimum concentration of GO nanosheets was achieved through incubating the UCNPs@SiO_2@apt at concentration of 0.2 mg/mL and 0.4 mg/mL at room temperature for 30 min, respectively, with GO nanosheets within the concentration range of 0.1−1.0 mg/mL under 808 nm excitation, and 0.1−0.5 mg/mL at 980 nm excitation. Finally, GO nanosheets together with UCNPs@SiO_2@apt were incubated under the above optimized experimental conditions to assemble NP detection sensor (UCNPs@SiO_2@apt-GO). The various incubation times among UCNPs@SiO_2@apt-GO sensor and NP estrogen were explored at 37 ℃. In the NP sensing experiment, UCNPs@SiO_2@apt-GO sensors that were developed under optimum experimental conditions, were incubated with NP at various concentrations for an optimized incubation time (1 h) at 37 ℃. At 980 nm or 808 nm laser excitation, UCL of the obtained sample was measured. The sensor specific recognition was evaluated by adding selected five estrogens including NP, PHE, PP, DEHP and BPA, respectively, to UCNPs@SiO_2@apt-GO. Same optimum conditions for experiment were followed to prepare the samples and the UCL spectra were measured at 980 nm excitation.

2.7 Detection of NP in Real Samples

UCNPs@SiO_2@apt sensor was applied to real sample of liquid milk to determine its reliability and sensitivity. After filtration by membrane with a pore size of 0.22 μm, 100 times the volume of liquid milk was diluted and then spiked with NP at concentrations of 10, 50, 200 ng/mL. The UCL measurements were carried out using an excitation laser at 980 nm to investigate the spiked real sample sensing application.

3 Results and Discussion

3.1 Characterization of UCNPs

$NaYF_4$: Yb/Er was utilized as the core nanoparticles because of high efficiency in NIR-to-visible UCL. Upon 980 nm irradiation, the NIR excitation energy was extracted by the Yb^{3+} ions which was further transferred to the upconverter ions (Er^{3+})[55]. The $NaYF_4$: Nd shell coating was used to protect the UCL from upconverter ions (Er^{3+}) in the core from surface quenching[56] and further enabling Nd^{3+} sensitization due to the high absorption capability of Nd^{3+} at 808 nm through the $^4I_{9/2} \rightarrow {}^4F_{5/2}$ transition and efficient interfacial energy transfer from Nd^{3+}-to-Yb^{3+}[57-59], upon which the UCL from activator (Er^{3+}) ion can be achieved (as shown in Fig. S1 in the Supporting Information). Furthermore, confining Nd^{3+} in the separate outer layer can remove strong unwanted interaction between Nd^{3+} and activator ion (Er^{3+})[56, 60]. Recently, the UCNPs with composition of $NaYF_4$@$NaYbF_4$: Tm@$NaYF_4$ were employed for the detection of 17β-estradiol estrogen[61]. In comparison, our presented UCNPs indicates multiple benefits such as Nd^{3+} or Yb^{3+} sensitization, highly efficient and strong green UCL due to protection of the upconverter ion (Er^{3+}) in the core, non-overheating effect and substantially enhancing the penetration depth for biological sensing ascribed to the 808 nm excitation exhibiting lower OH^- absorption than 980 nm.

The growth of $NaYF_4$: Yb/Er (20%/2%) core nanoparticles was followed by epitaxial shell deposition of $NaYF_4$: Nd (40%). TEM micrograph displays spherical morphology of the as-synthesized core nanoparticles and core-shell UCNPs in Fig. 2(a)−(b). The core nanoparticles are evenly distributed and monodispersed, with the mean diameter around 24.9 nm (Fig. S2(a)). Core-shell UCNPs exhibit a mean diameter of about 33.3 nm with a narrow size distribution (Fig. S2(b)). The elemental mapping and TEM of UCNPs are shown in Fig. 2(c)−(g), which confirms the presence of Er^{3+}, Nd^{3+}, Yb^{3+} and Y^{3+} in the core-shell structure. Fig. 2(h) presents the single particle HRTEM illustrating lattice fringes (d = 0.436 nm) which associated to the hexagonal structure (222) plane. The obtained XRD patterns (Fig. 2(i)) demonstrated that the hexagonal β-$NaYF_4$ phase (JCPDS standard card No. 16-0334) and the main diffraction peak locations are matched well which proves the good crystallinity of UCNPs.

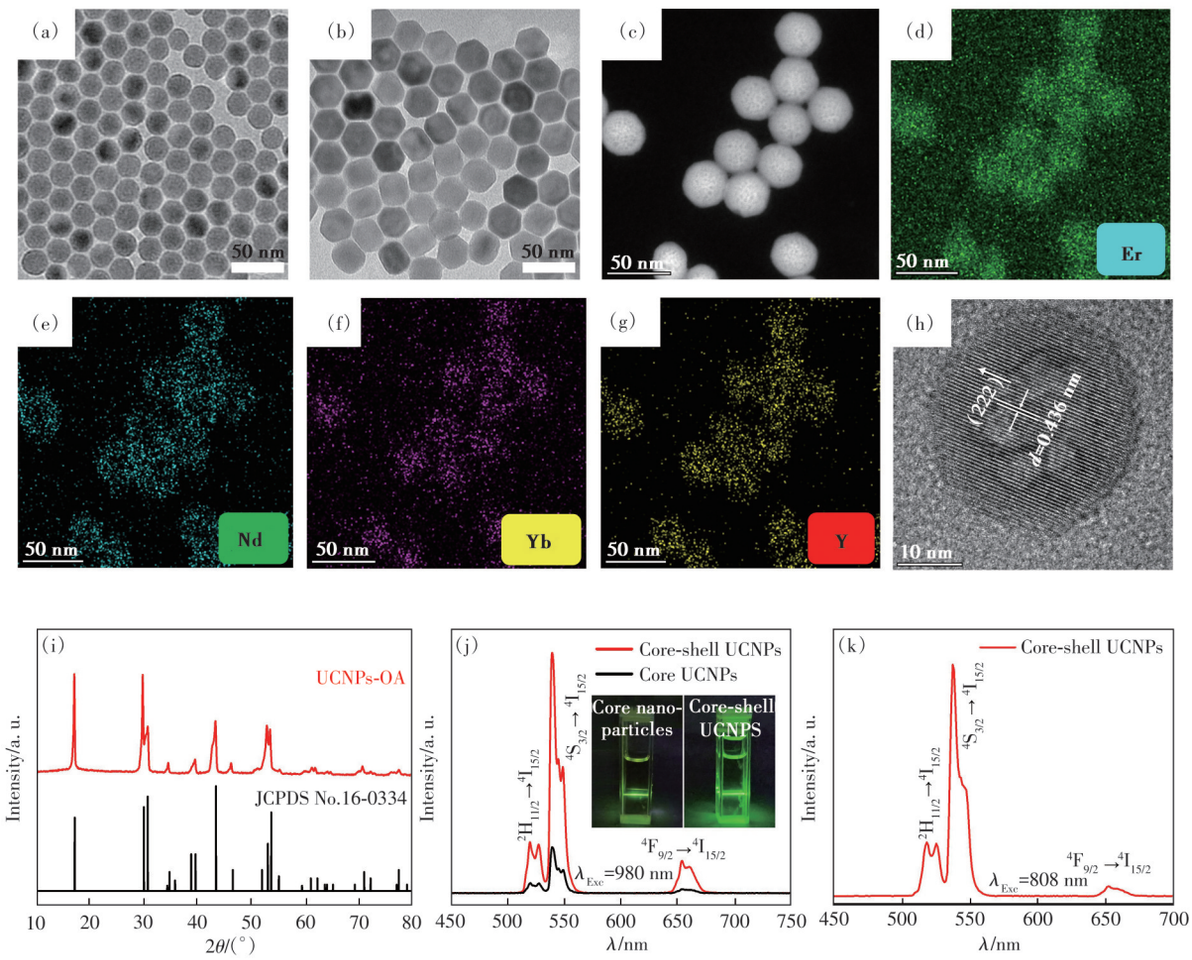

Fig.2 TEM micrographs of the as-prepared $NaYF_4$: Yb/Er core nanoparticles (a) and $NaYF_4$: Yb/Er@$NaYF_4$: Nd core-shell UCNPs (b). Representative TEM image of UCNPs for compositional analysis (c) and elemental mapping images of Er, Nd, Yb, and Y ((d)-(g)) of core-shell UCNPs. (h) HRTEM image of individual core-shell nanoparticle with *d*-spacing of 0.436 nm. (i) XRD pattern of UCNPs-OA. (j) UCL spectra of core nanoparticles and core-shell UCNPs at 980 nm excitation, with inset showing greatly enhanced UCL of core-shell UCNPs in contrast with core nanoparticles. (k) UCL spectrum of core-shell UCNPs under 808 nm NIR laser

The weak XRD peaks at 30.5° and 42.8° indicate the minor impurity phase possibly due to Y_2O_3 (JCPDS standard card No. 44-0399). The core nanoparticles ($NaYF_4$: Yb/Er) display the visible UCL upon 980 nm excitation (Fig. 2(j)). The core-shell ($NaYF_4$: Yb/Er@NaY_4: Nd) UCNPs exhibit the characteristic UCL with three major peaks centered at 521 nm, 540 nm and 654 nm which are associated with the Er^{3+} transitions of $^2H_{11/2}\rightarrow{}^4I_{15/2}$, $^4S_{3/2}\rightarrow{}^4I_{15/2}$, and $^4F_{9/2}\rightarrow{}^4I_{15/2}$, respectively, under 980 nm (Fig. 2(j)) or 808 nm (Fig. 2(k)) laser excitation. The shell coating of $NaYF_4$: Nd enables the core-shell UCNPs with significant enhancement in UCL intensity, as demonstrated in the inset of Fig. 2(j) for photographs comparison of the core nanoparticles and core-shell UCNPs at NIR (980 nm) excitation, which can be explained by the largely reduced surface quenching due to the solvent molecules, capping ligands, surface defects and other impurities[62].

3.2 Amino-SiO_2 Functionalized Core-shell UCNPs

To facilitate the development of an aqueous biosensing platform, the UCNPs require not only high UCL characteristics under NIR excitation (980 nm and 808 nm), but also good hydrophilicity, biocompatibility and NIR-transparency properties. Thus, surface modification of the UCNPs using the inert SiO_2 shell provides high water dispersibility because the as-synthesized UCNPs-OA are hydrophobic[37].

SiO_2 surface modification provides the potential to incorporate numerous functional groups on the surface of UCNPs[63]. The amino-functionalized SiO_2 layer offers binding site for aptamer conjugation and also increases the dispersibility of UCNPs in water[64].

The TEM image (Fig. 3(a)) shows uniform morphology of UCNPs@SiO_2-NH_2 which exhibit the particle size of ~36 nm in diameter. Considering the particle size of core-shell UCNPs at 33.3 nm (Fig. 2(b)), the SiO_2 shell thickness is estimated to be ~ 1.3 nm for coating on the surface of UCNPs. Fig. 3(b) presents the FT-IR spectra of UCNPs-OA and UCNPs@SiO_2-NH_2. The FT-IR broadband at 3 443 cm^{-1} of UCNPs-OA is attributed to stretching vibration of the —OH group[36,65]. The bands at 2 927 cm^{-1} and 2 854 cm^{-1} represent the asymmetric and symmetric stretching vibrations of the methylene (—CH_2—) group[66], respectively. The bands at 1 554 cm^{-1} and 1 461 cm^{-1} are associated to the asymmetric and symmetric stretching vibrations of the carboxylic group (—COO)[67], respectively. The peak appeared at 1 118 cm^{-1} is ascribed to C—O stretching vibration of carboxylic group. The absorption peak at 724 cm^{-1} is mainly attributed to —CH_2 rocking vibration[68]. After UCNPs surface modification by amino-SiO_2 layer, the UCNPs@SiO_2-NH_2 display significant decreased intensity for characteristic peaks at 2 927, 2 854, 1 554, 1 461 cm^{-1}, suggesting the OA ligand removal from the UCNPs surface. Furthermore, the UCNPs@SiO_2-NH_2 exhibit a strong band at 3 435 cm^{-1} that is assigned to OH group from silanol (Si—OH) group[52]. The peak at 1 632 cm^{-1} is originated to amino (—NH_2) group. The peaks at 1 072 cm^{-1} and 793 cm^{-1} are ascribed to asymmetric and symmetric stretching vibrations of Si—O—Si, respectively. The shoulder at 957 cm^{-1} is attributed to Si—OH and the peak at 460 cm^{-1} is associated to the bending vibration of Si—O—Si bond[41,68]. All the above-mentioned characteristic bands indicated that UCNPs surface was successfully modified with the amino-SiO_2 layer (UCNPs@SiO_2-NH_2). The contact angle measurements were carried out for UCNPs-OA and UCNPs@SiO_2-NH_2. Fig. 3(c) exhibits a water contact angle of 124.3° for hydrophobic UCNPs-OA. On the other hand, the water contact angle of UCNPs@SiO_2-NH_2 is 41.5° (Fig. 3(d)), suggesting efficient UCNPs water dispersion after surface coating of amino-SiO_2 layer. Based on these characteristics, the water-soluble UCNPs@SiO_2-NH_2 can be potentially used for the sensing of environmental, food or biological samples in aqueous media.

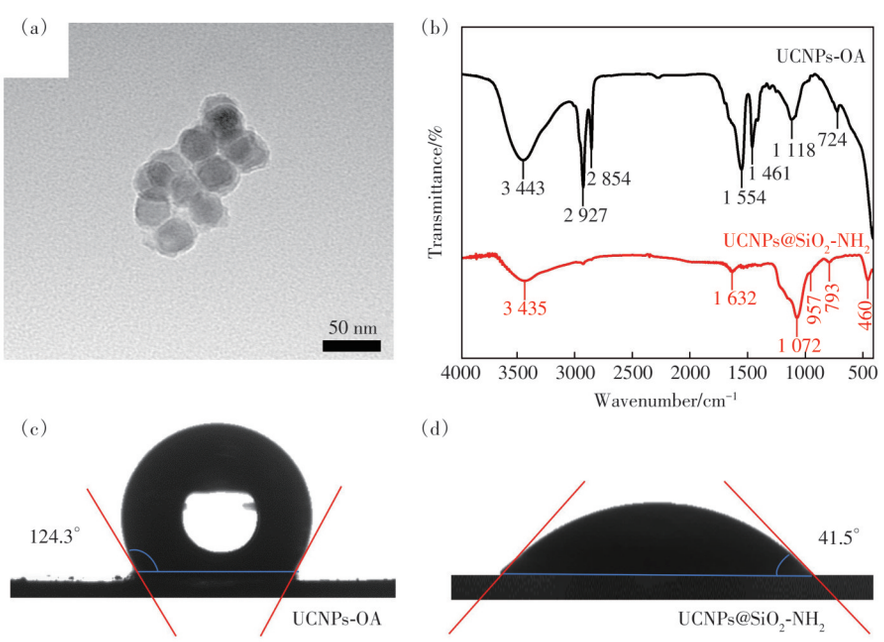

Fig.3　(a)TEM image of amino-SiO_2 modified $NaYF_4$:Yb/Er@$NaYF_4$:Nd core-shell UCNPs. (b)FT-IR spectra of UCNPs-OA and UCNPs@SiO_2-NH_2. (c)-(d)Water contact angle determination of UCNPs-OA and UCNPs@SiO_2-NH_2, respectively

3.3 Construction of UCNPs@SiO_2-GO Aptasensor for NP Sensing

Fig. 4(a) shows the UV-Vis absorption spectra of UCNPs@SiO_2-NH_2 before and after aptamers conjugation. Before aptamer conjugation, UCNPs@SiO_2-NH_2 exhibit no apparent absorption in range of 200–500 nm. The UCNPs@SiO_2@apt display absorption peak maxima at 265 nm that proves the successful conjugation of aptamer with UCNPs@SiO_2-NH_2[52]. Fig. 4(b) presents zeta-potentials for UCNPs@SiO_2-NH_2 and UCNPs@SiO_2@apt. The positive charge of (24.1 ± 0.7) mV observed for UCNPs@SiO_2-NH_2 reveals —NH_2 group which contains positive charge, is successfully functionalized on the surface of UCNPs@SiO_2. The single-stranded DNA aptamer conjugation with UCNPs@SiO_2-NH_2 could be justified by the negative zeta potential of (−3.3 ± 0.3) mV for UCNPs@SiO_2@apt, which is consistent with the

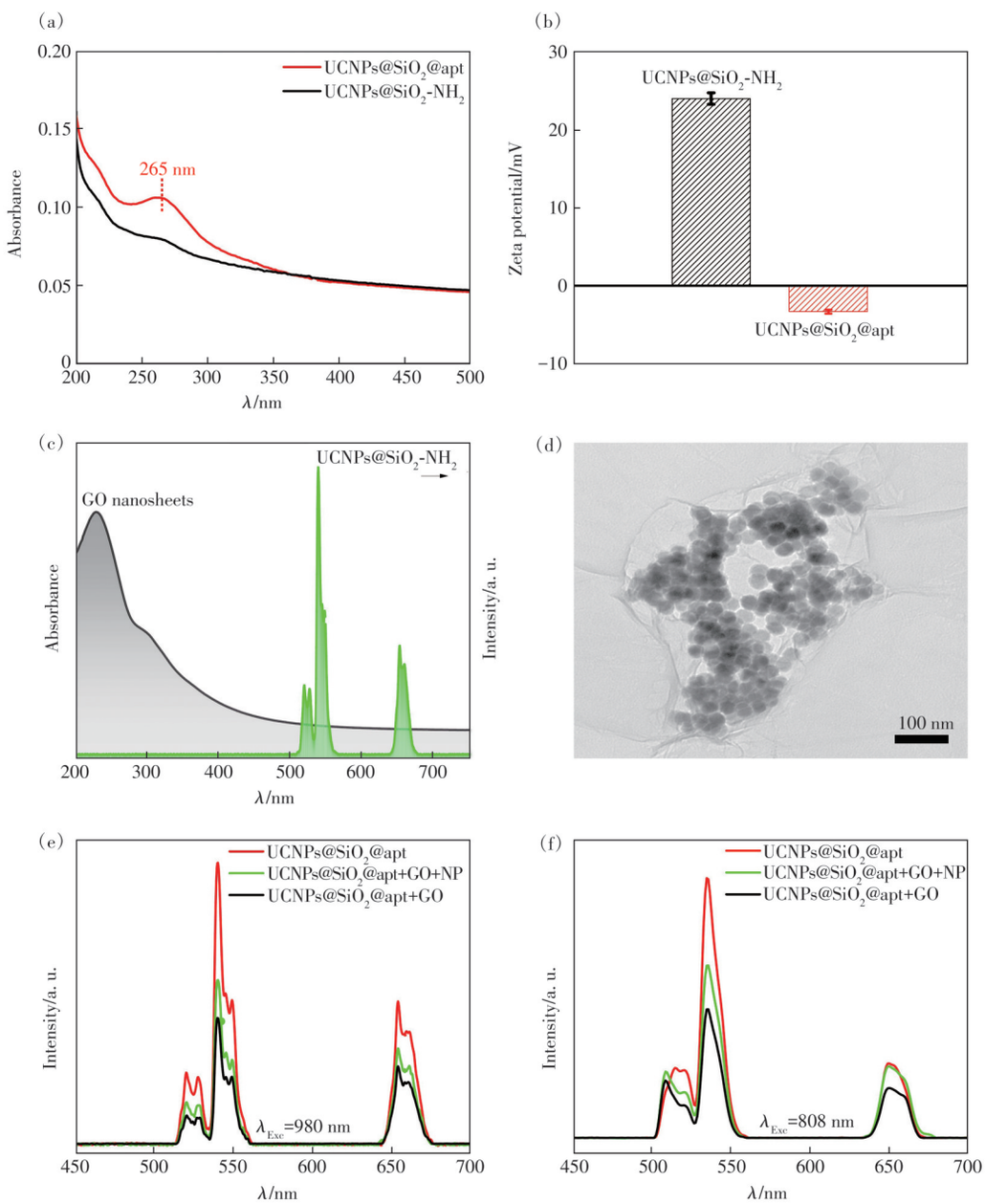

Fig.4 UV-Vis absorption spectra (a) and zeta potential (b) of UCNPs@SiO_2-NH_2 and UCNPs@SiO_2@apt. (c) UCL spectrum of UCNPs@SiO_2-NH_2 in comparison with the GO nanosheets UV-Vis absorption spectrum. (d) TEM image of GO nanosheets incubated with UCNPs@SiO_2@apt. UCL spectra of UCNPs@SiO_2@apt and UCNPs@SiO_2@apt-GO sensor with and without NP at 980 nm(e) and 808 nm(f) excitation, respectively

published result[69]. Fig. S3 shows the thin and uniformly spread two-dimensional shape of GO nanosheets with a broad surface area for potential binding with UCNPs@SiO_2@apt. The UV-Vis absorption spectrum of GO is presented in Fig. 4(c), which exhibits a broad range of strong absorption at 200–700 nm with a maxima at 230 nm[70]. The UCL spectrum of UCNPs@SiO_2-NH_2 (Fig. 4(c)) has characteristic peaks maxima at 521, 540, 654 nm corresponding to the transitions of $^2H_{11/2}\rightarrow{}^4I_{15/2}$, $^4S_{3/2}\rightarrow{}^4I_{15/2}$ and $^4F_{9/2}\rightarrow{}^4I_{15/2}$, respectively, from Er^{3+} under 980 nm excitation[55]. The significant overlap is observed between the UCL spectrum of UCNPs@SiO_2@apt and the UV-Vis spectrum of GO nanosheets. When addition of UCNPs@SiO_2@apt with GO nanosheets, the two-dimensional shape of GO nanosheets surface is attached with UCNPs@SiO_2@apt (Fig. 4(d)), causing the distance between the UCNPs@SiO_2@apt and GO nanosheets significantly decreased, corresponding to the π-π stacking interaction between nucleic acid chains from aptamer modified on UCNPs surface (UCNPs@SiO_2@apt) and GO nanosheets[50], leading to UCL quenching due to FRET from the energy donor (UCNPs@SiO_2@apt) to energy accepter (GO nanosheets)[71] (see Fig. S1). In addition to the fundamental requirement for the donor emission spectrum overlapped with the acceptor absorption spectrum, a non-radiative FRET process involves the energy donor-acceptor distance ⩽ 10 nm, whereas the radiative energy transfer can occur over relatively long distance beyond 10 nm based on the inner filter effect[26]. By considering the UCNPs@SiO_2-NH_2 diameter of 36 nm (Fig. 3(a)) and $NaYF_4$: Yb/Er core nanoparticles diameter of 24.9 nm (Fig. 2(a) and Fig. S2(a)), the thickness of $NaYF_4$: Nd and SiO_2 shells coated on $NaYF_4$: Yb/Er core nanoparticles was estimated to be ~ 5.5 nm, which supports that the FRET process occurs from Er^{3+} in the core of UCNPs to the GO nanosheets (see Fig. S1). In currently developed biosensor, the UCL of UCNPs@SiO_2@apt upon 980 nm (Fig. 4(e)) and 808 nm (Fig. 4(f)) excitation, is considerably quenched by GO nanosheets. When the NP estrogen analyte was added to UCNPs@SiO_2@apt-GO sensor, the UCL was recovered due to the predominant attachment of aptamer with NP that led to separation of GO nanosheets from UCNPs@SiO_2@apt. Therefore, NIR excitable UCNPs@SiO_2@apt-GO nanosensor could be potentially applied for turning-on sensing of NP estrogen.

3.4　Optimization Parameters for NP Detection

For the prepared UCNPs@SiO_2@apt-GO sensor, we systematically optimized the different experimental parameters, including the GO nanosheets incubation time with the UCNPs@SiO_2@apt, concentration of the GO nanosheets and the incubation time for NP estrogen with UCNPs@SiO_2@apt-GO sensor. Primarily, UCNPs@SiO_2@apt with GO nanosheets were incubated at different intervals of time and time-dependent UCL quenching was studied (Fig. S4(a)). From 1 min to 30 min of incubation, the UCL intensity was significantly decreased with negligible change after 30 min incubation time. Plotting incubation time against UCL quenching efficiency for UCNPs@SiO_2@apt with GO nanosheets addition is shown in Fig. S4(b). The interaction between UCNPs@SiO_2@apt with the GO nanosheets reaches balance after 30 min without apparent variation observed for UCL quenching efficiency. Hence, the optimized time of incubation was selected at 30 min for UCNPs@SiO_2@apt with GO nanosheets. To further explore the influence of GO nanosheets concentration on the UCL quenching, the GO nanosheets were incubated at different concentrations with UCNPs@SiO_2@apt for the optimum duration of time (30 min). With increasing concentration of GO nanosheets, the intensity of UCL decreased gradually and showed the maximum quenching concentration of GO nanosheets at 0.5 mg/mL and 1.0 mg/mL upon 980 nm (Fig. S5(a)) and 808 nm (Fig. S6(a)) laser excitation, respectively. The quenching efficiency increased gradually as the concentration of GO nanosheets increased in range of 0.1–0.5 mg/mL upon 980 nm laser excitation (Fig. S5(b)) and 0.1–1.0 mg/mL under 808 nm laser excitation (Fig. S6(b)), respectively. According to the recently reported FRET-based UCNPs sensor in Wen's group[52] and considering the inner filter effect,

the optimal concentration of GO nanosheets was chosen at 0.3 mg/mL and 0.4 mg/mL for UCNPs@SiO_2@apt-GO sensor, under NIR excitation wavelengths of 980 nm and 808 nm laser, to achieve UCL quenching efficiency at 49% and 51%, respectively. The UCNPs@SiO_2@apt-GO nanosensor was constructed based on the above-developed optimum experimental parameters and further incubated with NP at 37 ℃ for different time intervals to optimize the sensing performance. The UCL spectra in Fig. S7(a) show the luminescence recovery with increasing the time of incubation between NP estrogen and UCNPs@SiO_2@apt-GO. The relative UCL intensity increased progressively as the time of incubation increased, reached a maximum at 1 h and remained unchanged afterward (Fig. S7(b)). Thus, the optimum incubation time was selected at 1 h for the UCNPs@SiO_2@apt-GO sensor to further detect NP estrogen.

3.5 Quantitative Detection and Selectivity Assessment of NP

Under optimal conditions, the developed UCNPs@SiO_2@apt-GO sensor was utilized for the sensing of NP estrogen at concentrations ranging 5−200 ng/mL and 200−1 000 ng/mL upon 980 nm and 808 nm laser excitation, respectively. The UCL intensity was gradually restored with an increase in NP estrogen concentration under 980 nm (Fig. 5(a)) and 808 nm (Fig. S8(a)) laser excitation, respectively. The quantitative detection of NP estrogen was achieved by the relationship between the relative UCL intensities using the formula of $(I-I_0)/I_0$[72], where I_0 and I define the integrated UCL intensity of UCNPs@SiO_2@apt-GO sensor without and with NP estrogen addition, respectively, *versus* the concentration of NP estrogen. As shown in Fig. 5(b) and Fig. S8(b), the concentrations of the added NP estrogen in the range of 5−200 ng/mL and 200−1 000 ng/mL present a good linear correlation with the UCL intensities at 980 nm and 808 nm laser excitation, respectively. The results of the linear equation are: $y = 0.0030x + 0.1345$ with correlation coefficient $R^2 = 0.9991$ and $y = 0.0004x - 0.0731$ with $R^2 = 0.9790$ under 980 nm and 808 nm laser excitation, respectively. The estimated LOD is 4.2 ng/mL following the formula of $3\delta/S$[66], where S indicates the standard curve slope and δ is blank solution standard deviation with $n = 3$. UCNPs@SiO_2@apt-GO sensor possessed higher sensitivity, lower LOD, NIR excitation wavelength for negligible autofluorescence and convenient sensing approach, in comparison to earlier detection methods (Tab. S1). The UCL recovery efficiency of UCNPs@SiO_2@apt-GO sensor with presence of NP estrogen was further calculated to be 36.9% at NP concentration of 200 ng·mL^{-1} with 980 nm excitation (Fig. S9(a), (b)), and 42.8% at NP concentration of 1 000 ng·mL^{-1} with 808 nm excitation (Fig. S9(c), (d)). The selectivity experiment for the NP estrogen was performed by choosing four other estrogens including BPA, PP, DEHP and PHE. Fig. 5(c) demonstrates only the

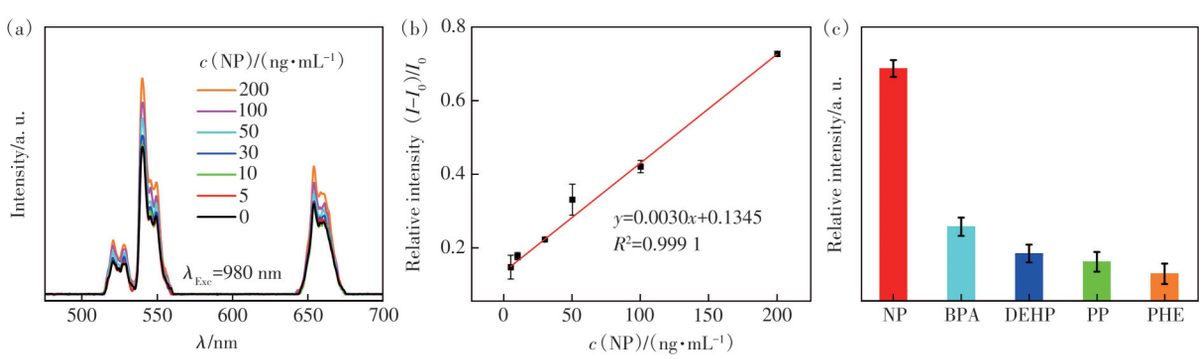

Fig.5 (a) UCL spectra of UCNPs@SiO_2@apt-GO sensor with increasing concentrations of NP estrogen under 980 nm laser excitation. (b) Relative UCL intensity for UCNPs@SiO_2@apt-GO sensor against concentration of NP with range of 5−200 ng/mL under 980 nm excitation. (c) Relative UCL intensities for UCNPs@SiO_2@apt-GO sensor with addition of different estrogens upon 980 nm laser excitation, showing good selectivity toward NP detection for developed UCNPs@SiO_2@apt-GO sensor

addition of NP estrogen resulting in efficient recovery in the UCL intensity, as compared to the other four estrogens at identical concentration of 200 ng/mL. These results validate the good selectivity of UCNPs@SiO_2@apt-GO sensor for NP estrogen detection.

3.6 Sensing of NP in Liquid Sample of Milk

To validate the practical applicability and reliability of our proposed sensing approach for real samples, standard addition method[73] was performed using spiked samples of NP with varying concentrations in real samples of milk. The commercially available liquid milk was used for testing with the addition of NP estrogen at concentrations of 10, 50, 200 ng/mL. The UCL intensity was increased with increasing NP concentration in milk samples, as shown in Fig. S10. Tab. 1 presents the recovery results of the spiked milk samples. The recoveries for the milk samples are 99.5%−105.5% and relative standard deviation (RSD) falls in the range of 1.5%−3.1%. All the findings validate the suggested approach based on the UCNPs@SiO_2@apt-GO sensor, providing a reliable alternative to existing fluorescence detection methods for a simple, convenient, selective and sensitive platform for monitoring NP estrogen in actual samples of milk.

Tab. 1　NP determination and recovery assay in real milk samples

Sample	NP spiked/ ($ng \cdot mL^{-1}$)	NP found/ ($ng \cdot mL^{-1}$)	NP recovery/%	RSD/% (n=3)
Milk1	10	10.5	104.7	1.8
Milk2	50	52.7	105.5	1.5
Milk3	200	199.1	99.5	3.1

4　Conclusion

This study develops a novel rare-earth fluoride-based upconversion nanosensor with NIR excitation for the selective and sensitive detection of NP estrogen. The nanosensor employs UCNPs ($NaYF_4$: Yb/Er@$NaYF_4$: Nd) as energy donor with NIR excitation, coupled with GO nanosheets as energy acceptor. The resulting UCNPs@SiO_2@apt-GO nanosensor, formed *via* π-π stacking interactions, exhibits efficient UCL quenching *via* FRET. Upon NP estrogen binding to the aptamer, the detachment of UCNPs@SiO_2@apt from GO nanosheets causes the UCL restoring, enabling linear detection ranges of 5−200 ng/mL and 200−1 000 ng/mL under 980 nm and 808 nm excitation, respectively, with LOD at 4.2 ng/mL. The sensor demonstrates successful NP estrogen detection in liquid milk samples, highlighting its potential for sensitive and selective turning-on sensing in food, environmental, and biological samples.

Supplementary Information and Response Letter are available for this paper at: http://cjl.lightpublishing.cn/thesisDetails#10.37188/CJL.20240187

References:

[1] TANG C J, HUANG X R, WANG H Y, *et al.* Mechanism investigation on the enhanced photocatalytic oxidation of nonylphenol on hydrophobic TiO_2 nanotubes [J]. *J. Hazard. Mater.*, 2020, 382: 121017.

[2] DE ALMEIDA W, MATEI J C, KITAMURA R S A, *et al.* Alkylphenols cause cytotoxicity and genotoxicity induced by oxidative stress in RTG-2 cell line [J]. *Chemosphere*, 2023, 313: 137387.

[3] YUAN X X, GAO N, GAO X, *et al.* Nanopyramid boron-doped diamond electrode realizing nanomolar detection limit of 4-nonylphenol [J]. *Sens. Actuators* B: *Chem.*, 2019, 281: 830-836.

[4] LI S N, XU W H, GONG L, *et al.* Subchronic nonylphenol exposure induced anxiety-like behavior and decreased expressions of regulators of synaptic plasticity in rats [J]. *Chemosphere*, 2021, 282: 130994.

[5] LIU T, DI Q N, SUN J H, *et al.* Effects of nonylphenol induced oxidative stress on apoptosis and autophagy in rat ovarian granulosa cells [J]. *Chemosphere*, 2020, 261: 127693.

[6] WU J Z, WEI W Y, AHMAD W, *et al.* Enhanced detection of endocrine disrupting chemicals in on-chip microfluidic biosensors using aptamer-mediated bridging flocculation and upconversion luminescence [J]. *J. Hazard. Mater.*, 2023, 458: 132025.

[7] YU M Z, WU L N, MIAO J N, *et al.* Titanium dioxide and polypyrrole molecularly imprinted polymer nanocomposites

based electrochemical sensor for highly selective detection of p-nonylphenol [J]. *Anal. Chim. Acta*, 2019, 1080: 84-94.

[8] WU Y C, ZHOU Z Y, FU H Y, *et al*. Metagenomic analysis of microbial community and gene function of anodic biofilm for nonylphenol removal in microbial fuel cells [J]. *J. Cleaner Prod.*, 2022, 374: 133895.

[9] SALGUEIRO-GONZÁLEZ N, CONCHA-GRAÑA E, TURNES-CAROU I, *et al*. Determination of alkylphenols and bisphenol A in seawater samples by dispersive liquid-liquid microextraction and liquid chromatography tandem mass spectrometry for compliance with environmental quality standards [J]. *J. Chromatogr.* A, 2012, 1223: 1-8.

[10] LUO S S, FANG L, WANG X W, *et al*. Determination of octylphenol and nonylphenol in aqueous sample using simultaneous derivatization and dispersive liquid-liquid microextraction followed by gas chromatography-mass spectrometry [J]. *J. Chromatogr.* A, 2010, 1217(43): 6762-6768.

[11] LIU X Y, ZHANG X Y, ZHANG H X, *et al*. A chemometric strategy for optimization of solid-phase microextraction: determination of bisphenol A and 4-nonylphenol with HPLC [J]. *J. Chromatogr. Sci.*, 2008, 46(7): 596-600.

[12] SHIH H K, SHU T Y, PONNUSAMY V K, *et al*. A novel fatty-acid-based in-tube dispersive liquid-liquid microextraction technique for the rapid determination of nonylphenol and 4-tert-octylphenol in aqueous samples using high-performance liquid chromatography-ultraviolet detection [J]. *Anal. Chim. Acta*, 2015, 854: 70-77.

[13] ZHOU Q X, GAO Y Y, XIE G H. Determination of bisphenol A, 4-n-nonylphenol, and 4-tert-octylphenol by temperature-controlled ionic liquid dispersive liquid-phase microextraction combined with high performance liquid chromatography-fluorescence detector [J]. *Talanta*, 2011, 85(3): 1598-1602.

[14] FU X C, DING B W, D'ALESSANDRO D. Fabrication strategies for metal-organic framework electrochemical biosensors and their applications [J]. *Coord. Chem. Rev.*, 2023, 475: 214814.

[15] TANG X D, YU H M, BUI B, *et al*. Nitrogen-doped fluorescence carbon dots as multi-mechanism detection for iodide and curcumin in biological and food samples [J]. *Bioact. Mater.*, 2021, 6(6): 1541-1554.

[16] TU Y J, WANG S P, YUAN X T, *et al*. Facile hydrothermal synthesis of nitrogen, phosphorus-doped fluorescent carbon dots for live/dead bacterial differentiation, cell imaging and two nitrophenols detection [J]. *Dyes Pigm.*, 2021, 184: 108761.

[17] JIANG L Y, LIU H J, LI M, *et al*. Surface molecular imprinting on CdTe quantum dots for fluorescence sensing of 4-nitrophenol [J]. *Anal. Methods*, 2016, 8(10): 2226-2232.

[18] DAI L X, ZHANG Q, MA Q Q, *et al*. Emerging near infrared fluorophore: dicyanoisophorone-based small-molecule fluorescent probes with large Stokes shifts for bioimaging [J]. *Coord. Chem. Rev.*, 2023, 489: 215193.

[19] ALEEM A R, LIU J, WANG J, *et al*. Selective sensing of Cu^{2+} and Fe^{3+} ions with Vis-excitation using fluorescent Eu^{3+}-induced aggregates of polysaccharides (EIAP) in mammalian cells and aqueous systems [J]. *J. Hazard. Mater.*, 2020, 399: 122991.

[20] CHEN Y, WANG S F, ZHANG F. Near-infrared luminescence high-contrast *in vivo* biomedical imaging [J]. *Nat. Rev. Bioeng.*, 2023, 1(1): 60-78.

[21] ALEEM A R, CHEN R H, WAN T H, *et al*. Highly water-soluble and biocompatible hyaluronic acid functionalized upconversion nanoparticles as ratiometric nanoprobes for label-free detection of nitrofuran and doxorubicin [J]. *Food Chem.*, 2024, 438: 137961.

[22] LUO Y X, LIU Q D, HE P, *et al*. Responsive regulation of energy transfer in lanthanide-doped nanomaterials dispersed in chiral nematic structure [J]. *Adv. Sci.*, 2023, 10(27): 2303235.

[23] SHANG Y F, CHEN T, MA T H, *et al*. Advanced lanthanide doped upconversion nanomaterials for lasing emission [J]. *J. Rare Earths*, 2022, 40(5): 687-695.

[24] HE Y, RAO H T, WANG J J, *et al*. Perovskite quantum dots modulating upconversion nanomaterials for cancer early detections [J]. *Cancer Nanotechnol.*, 2023, 14(1): 52.

[25] NIU Y Y, BAO Z H, GAO Y Q, *et al*. Brightening heavily doped upconversion nanoparticles by tuning characteristics of core-shell structures [J]. *J. Rare Earths*, 2024, 42(5): 947-954.

[26] ABDUL HAKEEM D, SU S S, MO Z R, *et al*. Upconversion luminescent nanomaterials: a promising new platform for food safety analysis [J]. *Crit. Rev. Food Sci. Nutr.*, 2022, 62(32): 8866-8907.

[27] LEE C, XU E Z, KWOCK K W C, *et al*. Indefinite and bidirectional near-infrared nanocrystal photoswitching [J]. *Nature*, 2023, 618(7967): 951-958.

[28] LIU H Y, LI J B, HU P F, *et al.* Facile synthesis of Er^{3+}/Tm^{3+} co-doped magnetic/luminescent nanosystems for possible bioimaging and therapy applications [J]. *J. Rare Earths*, 2022, 40(1): 11-19.

[29] PATEL M, MEENU M, PANDEY J K, *et al.* Recent development in upconversion nanoparticles and their application in optogenetics: a review [J]. *J. Rare Earths*, 2022, 40(6): 847-861.

[30] SHI S, CHEN J, WANG X W, *et al.* Biointerface engineering with nucleic acid materials for biosensing applications [J]. *Adv. Funct. Mater.*, 2022, 32(37): 2270210.

[31] WEI H L, ZHENG W L, ZHANG X, *et al.* Tuning near-infrared-to-ultraviolet upconversion in lanthanide-doped nanoparticles for biomedical applications [J]. *Adv. Opt. Mater.*, 2023, 11(11): 2201716.

[32] LIAO H Z, YE S, XU X L, *et al.* Dual excitable upconversion nanoparticle@polydopamine nanocomposite with intense red emission and efficient photothermal generation [J]. *J. Rare Earths*, 2023, 41(12): 1860-1868.

[33] BI S H, DENG Z M, HUANG J Q, *et al.* NIR-II responsive upconversion nanoprobe with simultaneously enhanced single-band red luminescence and phase/size control for bioimaging and photodynamic therapy [J]. *Adv. Mater.*, 2023, 35(7): 2207038.

[34] YAN L B, WANG Z M. Near-infrared optical sensing of biomacromolecules with upconversion nanoplatforms [J]. *Adv. Photonics Res.*, 2023, 4(1): 2200175.

[35] WEN H L, ZHU H, CHEN X, *et al.* Upconverting near-infrared light through energy management in core-shell-shell nanoparticles [J]. *Angew. Chem. Int. Ed.*, 2013, 52(50): 13419-13423.

[36] KONG W, SUN T Y, CHEN B, *et al.* A general strategy for ligand exchange on upconversion nanoparticles [J]. *Inorg. Chem.*, 2017, 56(2): 872-877.

[37] SEDLMEIER A, GORRIS H H. Surface modification and characterization of photon-upconverting nanoparticles for bioanalytical applications [J]. *Chem. Soc. Rev.*, 2015, 44(6): 1526-1560.

[38] HUANG Z, LIU Y H, CHEN Y, *et al.* Improving the performance of upconversion nanoprobe-based lateral flow immunoassays by supramolecular self-assembly core/shell strategies [J]. *Sens. Actuators* B: *Chem.*, 2020, 318: 128233.

[39] KOSTIV U, KOTELNIKOV I, PROKS V, *et al.* RGDS- and TAT-conjugated upconversion of $NaYF_4$: Yb^{3+}/Er^{3+} &SiO_2 nanoparticles: *in vitro* human epithelioid cervix carcinoma cellular uptake, imaging, and targeting [J]. *ACS Appl. Mater. Interfaces*, 2016, 8(31): 20422-20431.

[40] SHARMA K S, DUBEY A K, KUMAR C, *et al.* Mesoporous silica-coated upconversion nanoparticles assisted photodynamic therapy using 5-aminolevulinic acid: mechanistic and *in vivo* studies [J]. *ACS Appl. Bio Mater.*, 2022, 5(2): 583-597.

[41] SUN L L, WANG T, SUN Y Z, *et al.* Fluorescence resonance energy transfer between NH_2-$NaYF_4$: Yb, Er/$NaYF_4$@SiO_2 upconversion nanoparticles and gold nanoparticles for the detection of glutathione and cadmium ions [J]. *Talanta*, 2020, 207: 120294.

[42] TONG N B, VAN SI L, DUNG C T M, *et al.* Intense green upconversion in core-shell structured $NaYF_4$: Er, Yb@SiO_2 microparticles for anti-counterfeiting printing [J]. *Ceram. Int.*, 2023, 49(17): 28484-28491.

[43] LI H H, BEI Q Y, ZHANG W H, *et al.* Ultrasensitive fluorescence sensor for Hg^{2+} in food based on three-dimensional upconversion nanoclusters and aptamer-modulated thymine-Hg^{2+}-thymine strategy [J]. *Food Chem.*, 2023, 422: 136202.

[44] JAYASENA S D. Aptamers: an emerging class of molecules that rival antibodies in diagnostics [J]. *Clin. Chem.*, 1999, 45(9): 1628-1650.

[45] ZHANG D D, LUO T, CAI X Y, *et al.* Recent advances in nucleic acid signal amplification-based aptasensors for sensing mycotoxins [J]. *Chem. Commun.*, 2024, 60(36): 4745-4764.

[46] FU W, YIN J F, CAO H Q, *et al.* Non-blinking luminescence from charged single graphene quantum dots [J]. *Adv. Mater.*, 2023, 35(40): 2304074.

[47] MIN J, JUNG Y, AHN J, *et al.* Recent advances in biodegradable green electronic materials and sensor applications[J]. *Adv. Mater.*, 2023, 35(52): 2211273.

[48] LEWANDOWSKA-ANDRALOJC A, GACKA E, PEDZINSKI T, *et al.* Understanding structure-properties relationships of porphyrin linked to graphene oxide through π-π-stacking or covalent amide bonds [J]. *Sci. Rep.*, 2022, 12(1): 13420.

[49] ZHAO Q Z, DU P, WANG X Y, *et al.* Upconversion fluorescence resonance energy transfer aptasensors for H5N1 influenza

virus detection [J]. *ACS Omega*, 2021, 6(23): 15236-15245.

[50] MENDEZ-GONZALEZ D, CALDERÓN O G, MELLE S, *et al*. Contribution of resonance energy transfer to the luminescence quenching of upconversion nanoparticles with graphene oxide [J]. *J. Colloid Interface Sci.*, 2020, 575: 119-129.

[51] LI S, KANG Y, SHANG M D, *et al*. Highly sensitive and selective detection of Ochratoxin a using modified graphene oxide-aptamer sensors as well as application [J]. *Microchem. J.*, 2022, 179: 107449.

[52] WAN T H, SONG W, WEN H L, *et al*. The exploration of upconversion luminescence nanoprobes for tobramycin detection based on Förster resonance energy transfer [J]. *Mater. Today Adv.*, 2023, 19: 100409.

[53] CHO S W, LIM H J, CHUA B, *et al*. Single-stranded DNA probe paired aptasensor with extra dye binding sites to enhance its fluorescence response in the presence of a target compound [J]. *RSC Adv.*, 2021, 11(35): 21796-21804

[54] STÖBER W, FINK A, BOHN E. Controlled growth of monodisperse silica spheres in the micron size range [J]. *J. Colloid Interface Sci.*, 1968, 26(1): 62-69.

[55] SONG N, ZHOU B, YAN L, *et al*. Understanding the role of Yb^{3+} in the Nd/Yb coupled 808-nm-responsive upconversion [J]. *Front. Chem.*, 2019, 6: 673.

[56] ZHOU B, HUANG J S, YAN L, *et al*. Probing energy migration through precise control of interfacial energy transfer in nanostructure [J]. *Adv. Mater.*, 2019, 31(6): 1806308.

[57] DAI M M, FU Z L, WANG Z Y, *et al*. Sc^{3+}-induced double optimization strategies for boosting NIR-II luminescence and improving thermometer performance in CaF_2: Nd^{3+}, Nd^{3+}/Yb^{3+}@$NaYF_4$ nanocrystals [J]. *Chem. Eng. J.*, 2023, 452: 139133.

[58] XIE X J, GAO N Y, DENG R R, *et al*. Mechanistic investigation of photon upconversion in Nd^{3+}-sensitized core-shell nanoparticles [J]. *J. Am. Chem. Soc.*, 2013, 135(34): 12608-12611.

[59] ZHOU B, YAN L, TAO L L, *et al*. Enabling photon upconversion and precise control of donor-acceptor interaction through interfacial energy transfer [J]. *Adv. Sci.*, 2018, 5(3): 1700667.

[60] SU X, BAO Q H, ZHAN S P, *et al*. Extraordinary upconversion enhancement in hybrid metasurface by simultaneous excitation/emission band match [J]. *J. Alloys Compd.*, 2022, 925: 166761.

[61] WU J Z, AHMAD W, ZHANG J G, *et al*. Ratiometric upconversion-luminescence *in-situ* sampling aptasensing platform integrated with smartphone-based device for visual detection of 17β-estradiol [J]. *Sens. Actuators* B: *Chem.*, 2023, 390: 133999.

[62] SU Q Q, HAN S Y, XIE X J, *et al*. The effect of surface coating on energy migration-mediated upconversion [J]. *J. Am. Chem. Soc.*, 2012, 134(51): 20849-20857.

[63] LI T T, SHI S X, GOEL S, *et al*. Recent advancements in mesoporous silica nanoparticles towards therapeutic applications for cancer [J]. *Acta Biomater.*, 2019, 89: 1-13.

[64] OUYANG Q, WANG L, AHMAD W, *et al*. A highly sensitive detection of carbendazim pesticide in food based on the upconversion-MnO_2 luminescent resonance energy transfer biosensor [J]. *Food Chem.*, 2021, 349: 129157.

[65] WEN H L, WANG F. Lanthanide-doped nanoparticles: synthesis, property, and application [M]. TJONG S C. *Nanocrystalline Materials: Their Synthesis-Structure-Property Relationship and Applications*. Amsterdam: Elsevier, 2014.

[66] SU S S, MO Z R, TAN G Z, *et al*. PAA modified upconversion nanoparticles for highly selective and sensitive setection of Cu^{2+} Ions [J]. *Front. Chem.*, 2021, 8: 619764.

[67] WANG L, HARUNA S A, AHMAD W, *et al*. Tunable multiplexed fluorescence biosensing platform for simultaneous and selective detection of paraquat and carbendazim pesticides [J]. *Food Chem.*, 2022, 388: 132950.

[68] PREMARATNE W A P J, PRIYADARSHANA W M G I, GUNAWARDENA S H P, *et al*. Synthesis of nanosilica from paddy husk ash and their surface functionalization [J]. *J. Sci. Univ. Kelaniya*, 2014, 8: 33-48.

[69] KIM T, NAM K, KIM Y M, *et al*. DNA-assisted smart nanocarriers: progress, challenges, and opportunities [J]. *ACS Nano*, 2021, 15(2): 1942-1951.

[70] KALKAL A, PRADHAN R, PACKIRISAMY G. Gold nanoparticles modified reduced graphene oxide nanosheets based dual-quencher for highly sensitive detection of carcinoembryonic antigen [J]. *Int. J. Biol. Macromol.*, 2023, 242: 125157.

[71] LU C H, YANG H H, ZHU C L, *et al*. A graphene platform for sensing biomolecules [J]. *Angew. Chem. Int. Ed.*, 2009, 48(26): 4785-4787.

[72] WAN T H, ALEEM A R, HUANG S L, *et al.* Autofluorescence free functionalized upconversion nanoparticles-based turn-on aptasensor for highly sensitive and selective sensing of antibiotics [J]. *Mater. Today Adv.*, 2023, 17: 100326.

[73] 吴怡, 虞锐鹏, 陈海兰, 等. 电感耦合等离子体质谱(ICP-MS)法同时测定水系沉积物中痕量铅和砷 [J]. 中国无机分析化学, 2024, 14(11): 1471-1477.
WU Y, YU R P, CHEN H L, *et al.* Simultaneous determination of trace lead and arsenic in sediment by inductively coupled plasma mass spectrometry (ICP-MS) [J]. *Chin. J. Inorg. Anal. Chem.*, 2024, 14(11): 1471-1477. (in Chinese)

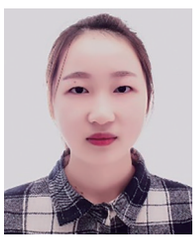

黄丝丽(1998–),女,湖北孝感人,硕士,2024年于广东工业大学获得硕士学位,主要从事无机稀土纳米材料合成及用于雌激素残留检测的研究。
E-mail: 1649009477@qq.com

陈伟(1965–),男,广西博白人,博士,教授,博士生导师,1992年于北京大学获得博士学位,主要从事纳米材料和芯片材料的研究。
E-mail: wei.chen03@xjtlu.edu.cn

温红丽(1978–),女,江西九江人,博士,教授,博士生导师,2012年于中国香港城市大学获得博士学位,主要从事稀土纳米材料及食品安全检测和荧光温度传感的研究。
E-mail: hongliwen@gdut.edu.cn

ABDUR Raheem Aleem(1989–),男,巴基斯坦人,博士,2021年于青岛大学获得博士学位,主要从事稀土纳米材料和无机/有机杂化发光材料的合成及用于环境危害元素传感、可穿戴生物传感器、生物成像和防伪应用研究。
E-mail: abdurraheemalem@hotmail.com